5R.1

STORM MORPHOLOGY AND RAINFALL CHARACTERISTICS OF TRMM PRECIPITATION FEATURES

Stephen W. Nesbitt*, Robert Cifelli, and Steven A. Rutledge
Colorado State Univerisity, Fort Collins, Colorado

1. Introduction

The launch of the Tropical Rainfall Measuring Mission (TRMM) satellite (Simpson et al. 1988; Kummerow et al. 1998) on 28 November 1997 has harbored an era of greatly increased understanding of Tropical precipitation systems. Largely through use of data from the TRMM Precipitation Radar (PR), allowing 3-D retrievals of radar reflectivity and precipitation rate, many works have examined, mainly separately, the horizontal and vertical structure of precipitating systems within the ±35° inclination orbit of TRMM. Combined with TRMM Microwave Imager (TMI) and Lightning Imaging Sensor (LIS) observations, Nesbitt et al. (2000), Toracinta et al. (2001), and Cecil et al. (2005) examined the radar reflectivity, 85 GHz ice scattering, and lightning flash rate characteristics of precipitation features (PFs, or areas of contiguous near-surface radar echo and 85 GHz ice scattering). These studies contrasted less convectively intense PFs over ocean regions with more convectively intense PFs over land regions as evidenced by differences in PR ETHs, TMI minimum 85 GHz brightness temperatures, and lightning flash rates. Studies have emphasized various portions of the convective intensity spectrum as well in their role in Tropical water budgets. Short and Nakamura (2000) highlight the high frequency of occurrence of shallow precipitation over the Tropical oceans while Takayabu (2002) showed the variation of the entire intensity spectrum of PR profiles. Petersen and Rutledge (2001) emphasized the regional direct relationship between increased ice and supercooled liquid water contents in convectively intense storms (as evidenced by increased frequency of higher PR reflecitivity values at greater heights) and LIS flash rates, owed to strong regional differences in the vertical structure of convection. Schumacher and Houze (2003a) examined the variability of bulk TRMM PR stratiform-rain fractions within the deep Tropics, finding strong regional gradients in this quantity. This finding implied significant differences in the large-scale response to precipitation among Tropical regions (Schumacher et al. 2004). However, hitherto the impact of precipitation system morphology has not been examined with TRMM, particularly with emphasis on how convective system organization impacts regional rainfall production.

This study aims to provide an important link between the vertical and horizontal structure of PFs and their rainfall characteristics through analysis using the "version 6" TRMM Precipitation Feature Database (Nesbitt and Zipser 2003), which incorporates not only PR and TMI observations, but also those from the Visible Infrared Radiation Scanner (VIRS) and LIS (the latter is not used in this study). The PF database is used to illustrate rainfall system morphology Tropicswide, highlighting regional differences in the organization of rainfall systems. In addition, this study examines the relationship of both horizontal size and proxies for convective intensity (vertical structure) to regional rainfall budgets. This study represents a preliminary step in model evaluation in putting forth an observational dataset that can be used to directly evaluate the performance of cloud-resolving models or GCM superparameterizations in representing rainfall system variability.

* *Corresponding author:* Dr. Stephen W. Nesbitt, Dept. of Atmospheric Science, Colorado State Univ., Fort Collins, CO 80523-1371
E-mail: snesbitt@atmos.colostate.edu

2. Data and Methods

2.1 The TRMM satellite

The reader is referred to Kummerow et al. (1998) for detailed information on the specifications of the TRMM PR, TMI, and VIRS instruments. This study uses version 6 TRMM 2A25, 2A12, and 1B01 products. More details about the TRMM algorithms may be found at http://tsdis.gsfc.nasa.gov.

2.2 The version 6 PF algorithm

The philosophy behind the "version 6" TRMM PF database is similar to the "version 5" database outlined in Nesbitt et al. (2000) and Nesbitt and Zipser (2003). TMI pixels are matched to PR pixels using a nearest neighbor approach. Once the matching is performed, the statistical properties of contiguous areas (including corner pixels) of PR near-surface reflectivity ≥ 20 dBZ or TMI 85-GHz PCT ≤ 250 K are compiled within the PR swath. A single-pixel minimum threshold (area 17.92 km^2), with that 1 pixel required to meet the PR threshold, is used instead of 4 pixels as in Nesbitt et al. (2000) as noise, clutter, and sidelobe contamination are largely nonexistent in version 6 2A25. Separate, but similar PF statistics of the TMI 2A12 surface rain pixels with rain rate > 0 mm h^{-1} are kept separately from those within the PR swath.

In addition to solely the PR and TMI data, the version 6 PF database includes VIRS 11.7 µm brightness temperatures, which are interpolated to the PR grid using a radial-basis approach, which was shown to be computationally efficient given the large number of interpolates in each orbit. Lightning Imaging Sensor (LIS) data are also included in the database, although not employed in this study.

This study uses three years of PF data extending including the calendar years of 1998, 1999, and 2000, as these were the only complete years of version 6 data available at present. PF characteristics are tabulated storm by storm, assigned to be over land or over ocean based upon their centroid location compared with a 0.5° resolution land-ocean mask. They are also gridded into $(2.5°)^2$ products assigned by their centroid location. Table 1 displays selected characteristics of features over land and ocean areas.

2.3 Determining PF horizontal dimension

The horizontal dimension of PFs is herein characterized using two methods. The number of raining PR pixels is counted and multiplied by the effective field of view of the instrument giving the raining area of each feature. In addition, an ellipse-fitting technique is employed whereby the major and minor axis lengths are calculated from the Eigenvalues of the mass distribution tensor of the raining points within each feature. Twice the major axis of the ellipse is recorded as the feature's maximum dimension (FMD).

Fig. 1 (a) and (b) show cumulative distribution functions (CDFs) of feature rain area (a) and FMD (b) for all features (solid line), and separately features that do not intersect the edge of the PR swath (dashed line), and features that do intersect the edge (solid line). As shown in panel a, 41% of features are 1 pixel (17.92 km^2) in area; 99.2% have areas less than 1000 km^2. The maximum PF area observed was 322883 km^2. In terms of FMD (in panel b), the same 41% of features

Table 1. Feature populations and characteristics over ocean and land.

	Ocean	Land
Number of features ($\times 10^3$)	15389	2733
Number fraction	.82	.18
R_{cond} (mm/hr)	2.71	2.81
R_{uncond} (mm dy^{-1})	2.48	2.02
A (km^2)	189	371
FMD (km)	17	21
Fraction of rain stratiform	.54	.48

which have 1 pixel areas have FMDs of 4.23 km ($\sqrt{17.92\ \mathrm{km}^2}$); 98.5% of features have FMDs less than 1000 km. The maximum FMD observed was 3782 km^2. When non-edge features are considered, their areal distributions and FMD are very similar in shape to the entire feature distribution, but is shifted slightly to smaller sizes while edge features tend to be significantly larger in area and FMD than the distribution of all features. In all, 9% of features from the 3-yr data base intersect the edge.

Fig. 2 shows (a) the number fraction and (b) rainfall fraction of features intersecting the edge of the swath. Both quantities are maximized in the ITCZ and in mid-latitude areas. The number fraction of edge features is higher over land than ocean because of a lower fraction of smaller features over land (which have a higher probability of intersecting the swath edge. In all, the 9% of features that intersect the edge of the PR swath contribute 42% of rainfall to the PR estimates. The rainfall fraction of edge features is highest at mid-latitudes (over 60% in many areas) where the PR swath is undoubtedly slicing elongated frontal PFs, and lowest in the subtropical highs where PFs are small and less than 10% of rainfall occurs in edge features.

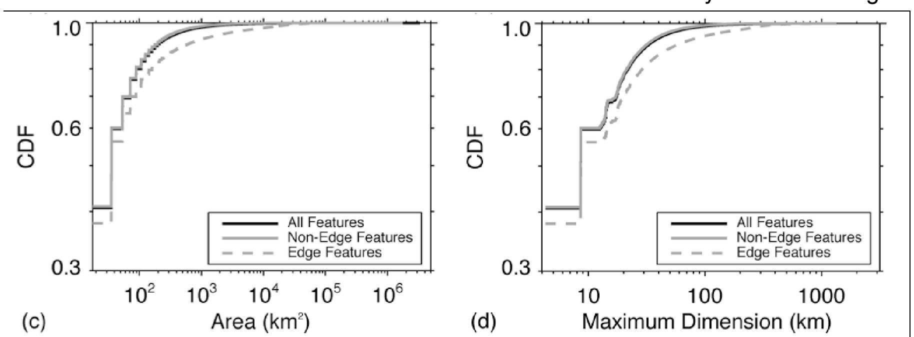

Fig. 1: CDFs of (a) feature area and (b) FMD for all features (dark solid lines), non-edge features (grey solid lines), and edge features (dashed grey lines).

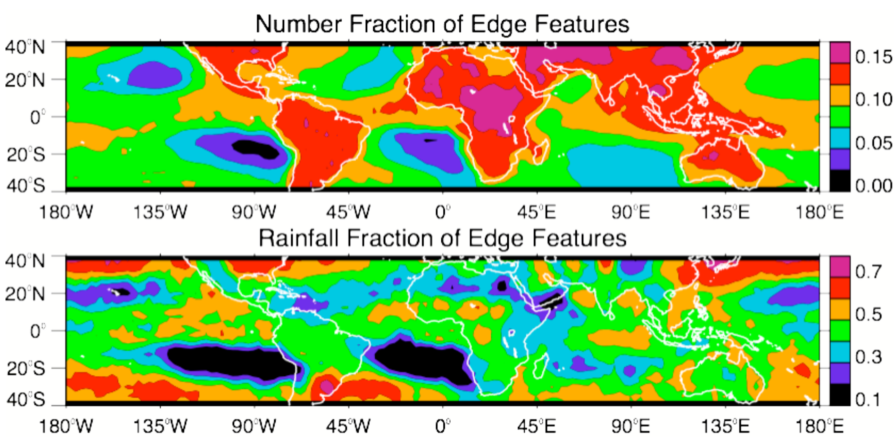

Fig. 2: Contour maps of: (a) the number fraction of edge features (b) the rainfall fraction of edge features.

3. Comparisons of PR PF size distributions with other estimates

To examine the impact of the PR's relatively small swath width on precipitation feature size characteristics, the PR-derived features were compared with TMI-derived feature areas (with a swath width 3.5 times the PR's) within the TMI surface rain field (rain rate > 0 mm h^{-1}) for the same time period as the PR results. Fig. 3 shows the fraction of total feature area within each area bin and CDFs of feature area. Note that the coarser resolution

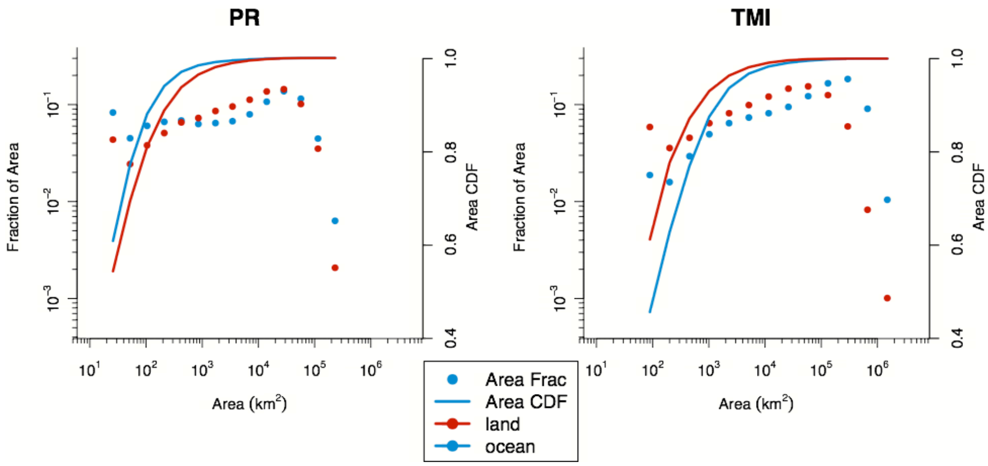

Fig. 3: Fraction of features within each area bin (dots) and CDFs of feature area (lines) for the PR PFs (left) and TMI PFs (right) over ocean (blue) and land (red).

of the TMI pixels (59.6 km^2) shifts the low end of the TMI distributions towards larger values (for areas < 500 km^2).

As indicated by the fraction of area by feature size distributions, the PR and TMI distributions are very similar overall, given the differences in minimum feature size (at the lower end of the distribution) and swath width (at the upper end of the distribution). Importantly, the slope of these PR and TMI PF area distributions shown by their PDFs are nearly identical, up to an apparent truncation point at nearly 30 000 km^2 in the PR distribution, while the TMI distribution maintains the same slope up until nearly 200 000 km^2. These results suggest that the PR swath width limit is not drastically biasing the precipitation feature size distribution below the apparent truncation point.

The PR distribution has more rain area portioned to smaller features and large features over ocean than over land. The TMI shows a different trend: over land (ocean) a higher relative portion of the total raining area is assigned to smaller (larger) features, with a crossover around 100 000 km^2. The TMI results are consistent with previous work using IR data (Machado and Rossow (1993).

The CDFs show that TMI features are generally larger in area than PR features, again consistent with the swath width differences and differences in pixel sizes. However, the relative area difference between land and ocean regions is switched between TMI and PR features. The PR (TMI) finds that continental (oceanic) features are larger. The fact that the PR retrievals use much more similar physics over both land and ocean relative to the TMI (which also have larger effective pixel sizes), it is presumed that the PR land-ocean differences are more realistic. For this reason, the remainder of this study will focus on analysis with the PR, noting that the feature size distribution is truncated as shown above.

4. PF morphology and rainfall

Regional distributions of 3-year mean feature area and FMD determined from PR PFs are contoured (on a log scale) in Fig. 4 top and bottom respectively. In a broad sense, both measures show maxima at the climatologi-

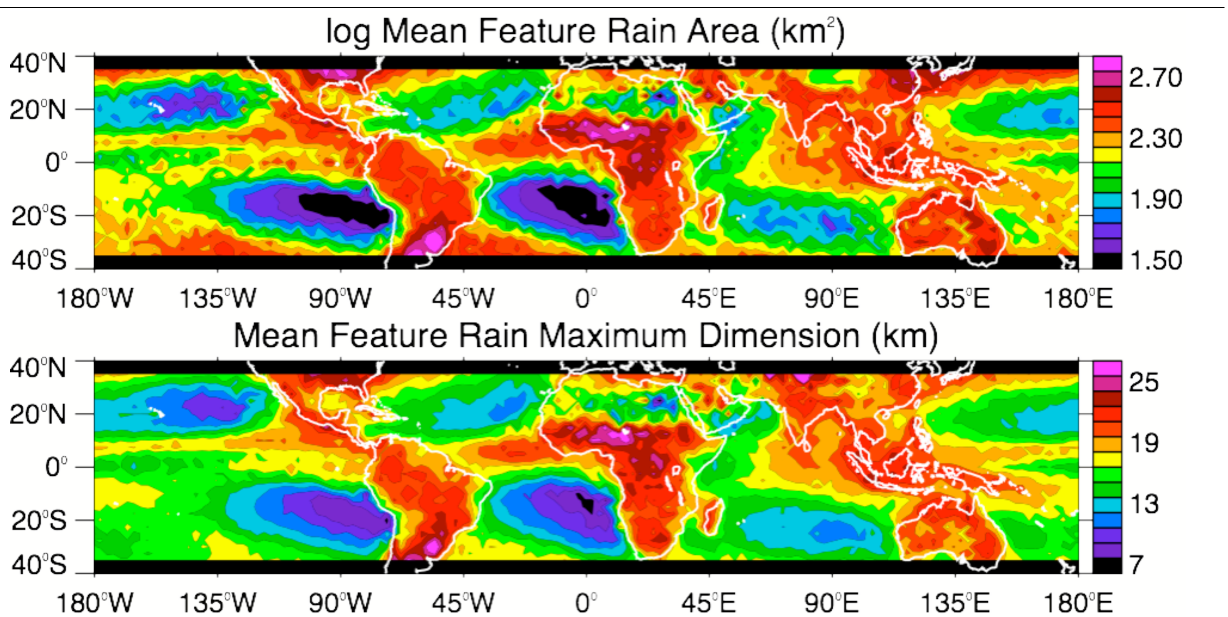

Fig. 4: (top) Log-contour map of mean feature rain area (km^2), (bottom) contour map of mean feature maximum dimension (km).

cal location of the ITCZ and in the Subtropics. Within the Tropics, the Sahel region in Africa stands out where features are largest by both measures. Moreover, the Congo basin has regions where features, on average, exceed 500 km^2; no regions within the Amazon basin or Maritime Continent exceed this value on average. Cross-Pacific variability includes larger features on each end of the ITCZ, with a minimum near 180° longitude. In the Subtropics, the semi-permanent highs near ±20° latitude lead to areas where oceanic PFs are small by both dimensional measures. However, with the exceptions of the Sahara and the Arabian Peninsula, all continental areas have features larger than their surrounding oceanic counterparts. In the Midlatitudes, feature sizes are generally higher than in lower latitudes, with maxima in both feature area and FMD over the La Plata Basin and the USA. Subtropical Oceanic maxima tend to be downstream of the continents where SSTs tend to be climatologically warmest and the influence of extratropical cyclones is likely the greatest.

4.1 Rainfall and horizontal structure

Fig. 5a compares probability distribution functions (PDFs) of the frequency of occurrence and rainfall fraction as a function of rain area and FMD over ocean and land areas. As shown in Fig. 3, ocean features are more numerous than land features at the small end of the area distribution, while the reverse is true at the larger end of the distribution. The fractional rain volume contribution by feature area shows three regimes, whereby a mid range (bracketed by areas of 400 and 20000 km^2) has higher relative contribution from features over land than over ocean; with the opposite true for small and large features on both sides of this range. The plot showing number and rainfall contributions by FMD show a similar distribution, with the three regimes of rain volume contribution by FMD showing up in panel (b) as in (a) in terms of area.

4.2 Rainfall and vertical structure

To examine the effects of PF vertical structure on rainfall, Fig. 6 shows the number and rainfall fraction of features as a function of 4 proxies of PF maximum convective depth and/or intensity over ocean and land surfaces. Panel (a) and (b) show the above quantities as a function of maximum 17 and 30 dBZ ETH within each feature, respectively (note that features without 30 dBZ echo are plotted along the ordinate in b). In terms of number fraction, the distribution is shifted to higher heights for features over land relative to the ocean distribution, with a modal value at nearly 6 km (4.5 km) at 17 dBZ (30 dBZ) over land, while over ocean the modal value is near 2.5 km in both the 17 and 30 dBZ ETH. Several studies have shown that continental rainfall originates significantly more often from features with vertical structures of sufficient intensity to produce lightning (Zipser and Lutz 1994; Nesbitt et al. 2000; Toracinta et al. 2000; Petersen and Rutledge 2001; Christian et al. 2003; Cecil et al. 2005).

When examining the rainfall distributions in context with the number distributions over land and ocean, note that the large number of shallow features with 17 dBZ ETHs below the freezing level do not contribute more than 15% of the rainfall over ocean or more than 5% of the rainfall over land. The rainfall distributions are displaced in a land-ocean sense just as their number distributions, with a higher fraction of rainfall over land coming from more vertically developed features (where mixed-phase processes are involved in rainfall production). Note the trimodal distribution in rainfall by 17 dBZ echo top over ocean, with relative maxima in rainfall contributions from features with ETHs below the freezing level, at 8.5-10

(below) Fig. 5: Number fraction (dashed lines) and rain volume fraction (solid lines) of features over ocean (dark lines) and land (grey lines) as a function of (a) rain area (km^2) and (b) FMD (km).

(right) Fig. 6: . Number fraction (dashed lines) and rain volume fraction (solid lines) of features over ocean (dark lines) and land (grey lines) as a function of (a) PR maximum 17 dBZ ETH (km), (b) PR maximum 30 dBZ ETH (km), (c) VIRS minimum IR T_b (°C), and (d) TMI minimum 85 GHZ PCT (K).

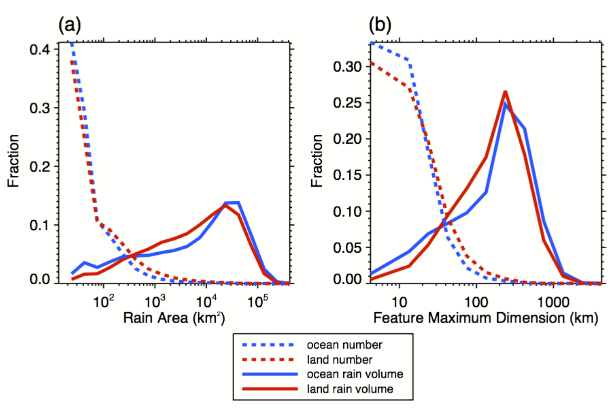

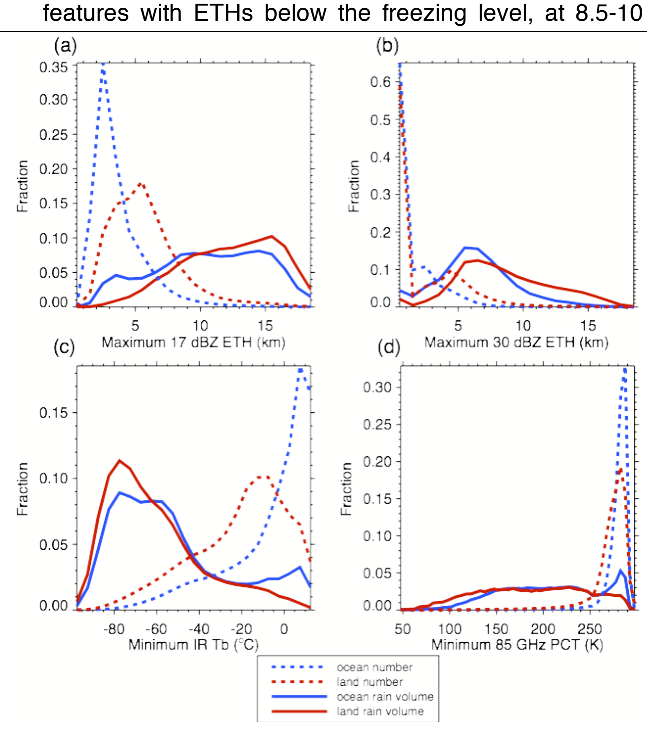

km, and at roughly 15 km. This structure is similar to the trade wind, cumulus congestus, and deep convective populations noted by Johnson et al. (1999) in the Tropical Ocean Global Atmosphere-Coupled Ocean Atmosphere Response Experiment (TOGA-COARE) ship-based radar dataset. Over land, the rainfall peak from below the freezing level is not nearly as evident as over ocean, however (perhaps due to capping inversions or differences in CCN concentrations), more prominent peaks at 10-12 and 15-17 km are present in the land 17 dBZ ETH distributions. At 30 dBZ in (b), about 30% of oceanic and continental rainfall falls with echo tops between 5.5 and 6.5 km; the ocean distribution (similar to that found in DeMott and Rutledge 1998) falls off more quickly than the land distribution, which has more than 5% rainfall contributions from features up to nearly 13 km. These results illustrate the relative importance of mixed phase processes to rainfall in the land PF's relative to their oceanic counterparts.

Panels (c) and (d) of Fig. 6 show the number and rainfall fraction from two other measures of convective vertical development, minimum VIRS IR T_b and minimum TMI 85 GHz PCT. Again, distinct differences exist among land and ocean locations, especially above 0°C in the IR distributions and 260 K in the 85 GHz distributions. Consistent with the ETH proxies described above, the large portion of features with warm T_b s in the IR and at 85 GHz do not produce significant rainfall contributions. The IR number distribution over ocean has a peak warmer than 0°C which does cause a small rainfall peak, while over land the modal IR T_b is -10°C, corresponding with a small relative increase in rainfall contribution. Overall, the IR-land frequency histogram is shifted towards colder T_b s; and the rainfall distributions show a single rainfall peak at -70°C over land, while ocean rainfall contribution peaks, in addition to the one at previously mentioned at 15°C, occur at -50°C to -55°C and -70°C. Distributions at 85 GHz are similar in general, with higher fractional number and rainfall contributions at lower 85 GHz PCTs over land; thus relatively higher optical depths of ice are responsible for rainfall processes over land, especially above 260 K (which is reflected in lightning-rainfall differences previously discussed).

5. Rainfall contribution by feature type

In order to examine variability in relevant regional rainfall characteristics, features are separated into 4 classes, each with characteristic diabatic heating profiles, based upon their PR horizontal and vertical structure. Table 2 lists the criteria of each of the feature types.

Table 2. FMD and ETH criteria for the four feature types examined in this study.

PF Type	FMD criteria	ETH criteria
Shallow (S)	-	ETH≤4.5 km (MSL)
Small “Cold” (SC)	FMD<100 km	ETH>4.5 km
Large “Mid-level” (LM)	FMD≥100 km	4.5>ETH>9.5 km
MCS	FMD≥100 km	ETH≥9.5 km

Shallow features (abbreviated by S) are those that have no measurable PR reflectivity (>17 dBZ) at heights greater than 4.5 km MSL; it is recognized that there may be mixed or ice phase precipitation above this height not intense enough or not large enough in dimension to fill a PR resolution volume, or the freezing level may be lowered in the Subtropics. Precipitation from systems in this category, however, likely have a large warm rain component (i.e. dominated by collision-coalescence mechanisms at temperatures > 0°C), and have latent heating confined to these shallow cloud depths. Small “cold” (SC) features range from individual cumulus congestus clusters to organized deep convective clusters < 100 km in EMD and likely have a relatively small stratiform rain (and stratiform-mode latent heating) contribution, and mixed and ice phase precipitation occurring. Large “Mid-level” features (LM) are large in size, but do not meet the ETH criteria at 9.5 km. These features consist of weak or dissipating MCSs (and frontal systems in the Subtropics). They have a mix of convective and stratiform rain heating profiles, but are likely dominated by a stratiform rain and latent heating component due to the absence of deep convection according to the PR criteria selected here. The MCS definition used in this study aims to follow the Houze (1993) definition, rather than the Nesbitt et al. (2000) definition since radar FMD and ETH criteria are, in principle, more objective than 85 GHz ice scattering areal coverage and intensity criteria over land and ocean where modal convective intensity differences (and storms' ability to loft precipitation-sized ice particles into the anvil) may affect the ice-scattering MCS classification. MCSs have a deep convective and stratiform heating profile (Houze 1989), however relative contributions to total heating by MCSs vary by meteorological regime that lead to modal changes in convective intensity and convective-stratiform rain partioning. The aim of this section is to quantify the relative and absolute contribution of these feature types to estimate how the superposition of these varying rainfall and latent heating regimes vary regionally.

To contrast bulk land-ocean differences in precipitation system type, Table 3 shows feature populations, rainfall fraction, and horizontal size characteristics mean area and FMD for the 4 feature types outlined above. Consistent with Short and Nakamura (2000), S features dominate the population over ocean; however this feature type occurs less frequently than SC features over land. MCSs are slightly more (nearly twice as) numerous than LM features over ocean (land). Despite indications that oceanic features have less convective intensity (i.e., less robust vertical structure) than continental features, consistent with differences in bulk buoyancy profiles (Fig. 9, Nesbitt et al. 2000; Toracinta et al. 2001; Petersen and Rutledge 2001; Cecil et al. 2005), all categories of features are larger in terms of horizontal

Table 3. Populations and horizontal extent characteristics over land and ocean for the four feature types.

	S		SC		LM		MCS	
	Ocean	Land	Ocean	Land	Ocean	Land	Ocean	Land
Number of features ($\times 10^3$)	12108	1067	3101	1600	82	21	98	45
Number fraction	.787	.391	.202	.585	.005	.008	.006	.016
Mean area (km^2)	50	42	205	170	6358	5605	11166	9445
Mean EMD (km)	12	10	26	21	175	170	215	205

structure (both mean area and mean FMD) over ocean than over land.

The fraction of rainfall by the four feature types in annual-average 2.5° boxes (smoothed with a 1:10:1 box filter in both dimensions) is contoured in Fig. 7. While feature populations are dominated by S features as shown above, Fig. 7 shows that rainfall (and bulk latent heating) are dominated by the MCSs in most heavily raining areas of the Tropics and Subtropics. The La Plata Basin sees MCS rainfall contributions nearing 90 percent of total rainfall; the Sahel, Congo Basin, south central US (consistent with Fritsch et al. 1986), and the west coast of Central America/nearby East Pacific see MCS contributions exceeding 70 percent. Most other heavily raining Tropical areas have MCS rainfall contributions of at least 50 percent over both land and ocean. Note the interesting cross-Pacific variability, however. MCS contributions gradually fall off from high fractions in the extreme East Pacific to values near 50 percent in the Central Pacific. MCS rainfall is replaced by increased fractions in W, SC, and LM features near the dateline. This indicates that features are less vertically intense and horizontally developed in the central Pacific relative to the East. Continuing further to the West Pacific, MCS and SC fractions increase above 70 and 20 percent, respectively. LM and S fractions decrease in compensation to very small fractions as one proceeds to the Maritime Continent. This Cross-Pacific variability in PF type has important ramifications for the water cycle over the Pacific and large-scale circulation in the region (Schumacher et al. 2004).

To examine how rainfall by feature type varies as a function of total rainfall, Fig. 8 shows plots of the rain volume fraction (a and b) and unconditional rain rate contribution (c and d, on a log-log axis) by each feature type as a function of total unconditional rain rate. Overlain on (a) and (b) is a least-squares fit logarithmic model (i.e., y=A+Blog(x)) for illustrative purposes, R^2 values for each model are also shown. Over ocean (a) at low rain rates (< 1 mm dy^{-1}), S features dominate the contribution to total rainfall, while over land the low intensity rain producers are largely SC features and MCSs. Fig. 7 shows that areas dominated by lightly raining SC features mainly exist over the oceanic subtropical highs and continental mountainous areas and deserts. There are also areas where LM features produce around 50 percent of the total ocean rainfall at an unconditional rain rate around 1 mm dy^{-1}; these are areas where frontal precipitation likely plays a role in the Subtropics. At higher unconditional rain rates (in the 1-3 mm dy^{-1} range) over ocean, both MCSs and SC features become more important in the rainfall budget. Over land, MCSs tend to contribute more rainfall while SC features tend to decrease in fractional rainfall contribution.

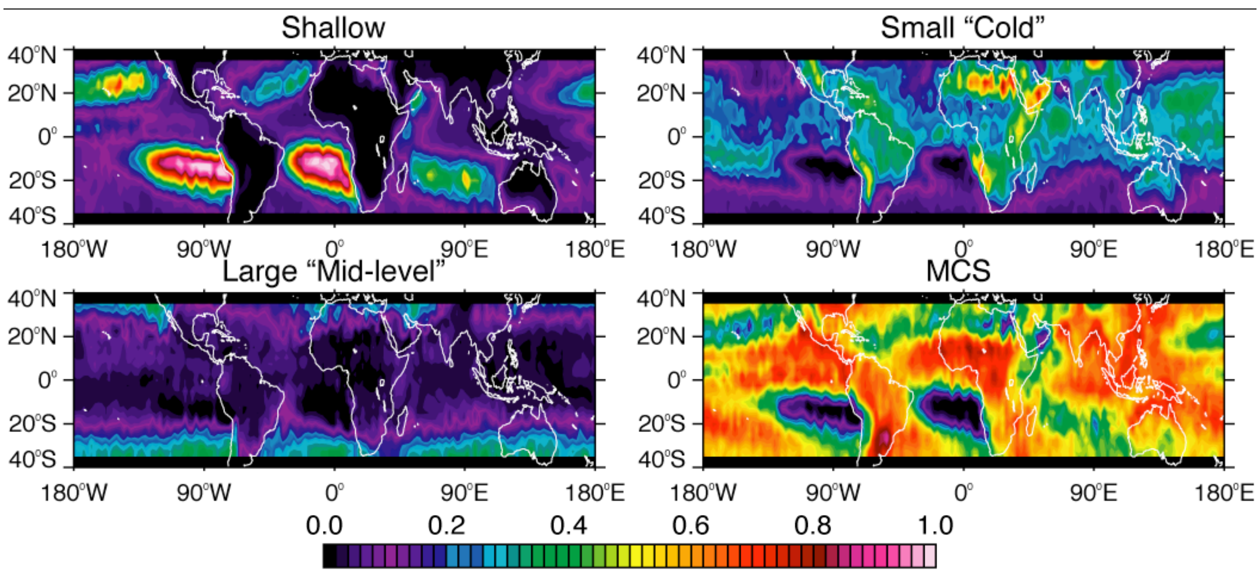

Fig. 7. Shaded contour map of fraction of rainfall by feature type.

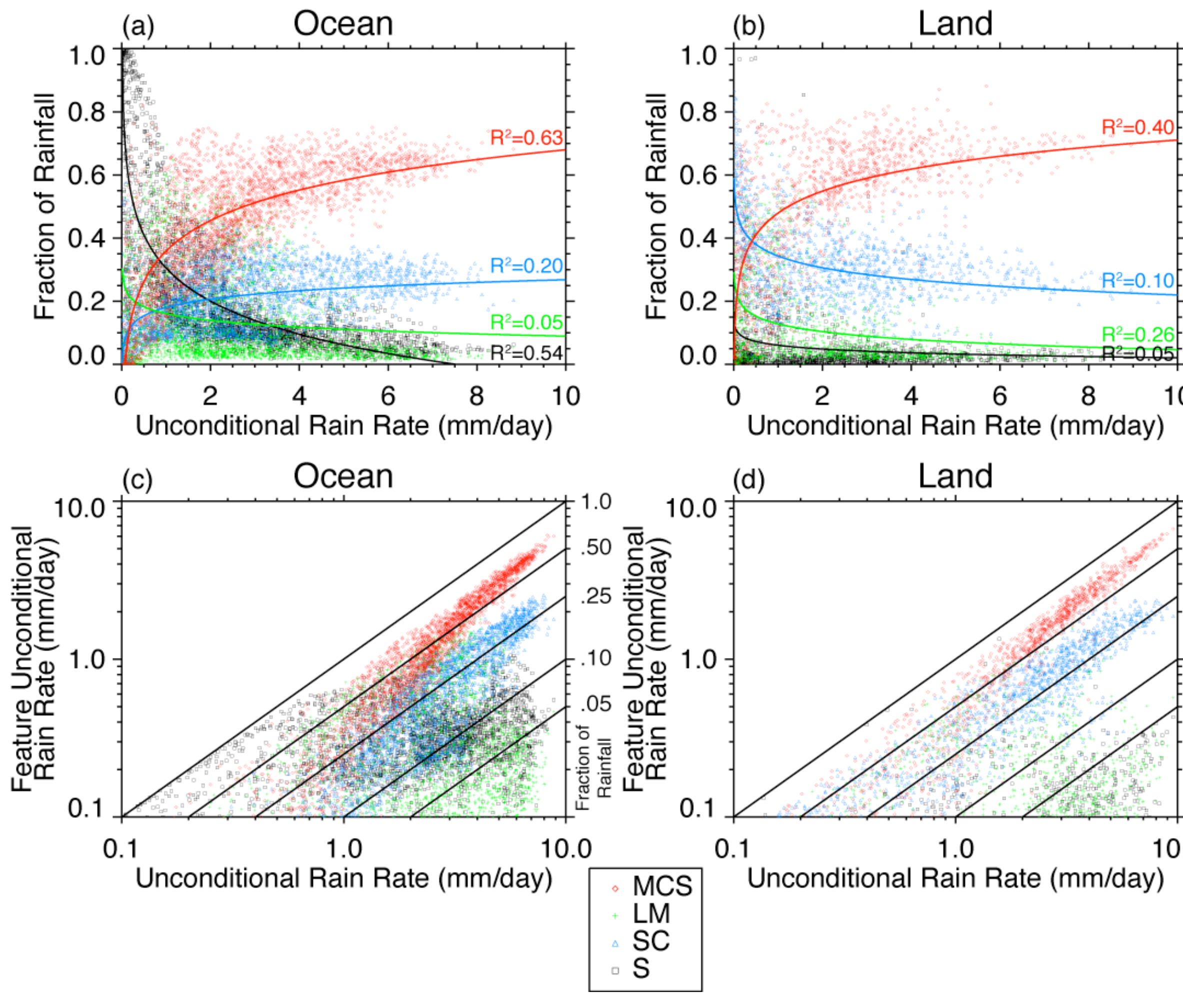

Fig. 8. Scatter diagrams of fraction of rainfall by feature type (see legend at bottom) versus unconditional rain rate (mm dy^{-1}) over ocean (a) and land (b). A best-fit logarithmic model appears for each feature type in the same color (with corresponding squared correlation coefficent values noted at right). Similarly, scatter diagrams of feature unconditional rain rate (mm dy^{-1}) (see legend at bottom) versus total unconditional rain rate (mm dy^{-1}) in 2.5 deg grid boxes over ocean (a) and land (b). Fraction of rain contours appear on the diagram and are labeled at right.

Above 3 mm dy^{-1} over both land and ocean, the separation of feature types becomes much more clear (and constant) in terms of fractional rainfall contribution. MCSs dominate the rainfall budget over both land and ocean (contributing a nearly constant fraction of rainfall as a function of total rain rate), with land areas having higher extreme and slightly higher modal values. SC rainfall fractions settle out to near a value of 0.25 to 0.30, higher (lower) than values at lower rain rates over ocean (land). LM and S features contribute less than 20 and 10 percent of total rainfall over ocean and land, respectively, for most total rain rates > 3 mm dy^{-1}.

The log-log plots of feature unconditional rain rate versus total rain rate in c and d of Fig. 8 show that S features rarely contribute more than 1 mm dy^{-1} over ocean, and 0.4 mm dy^{-1} over land, even in areas with high total rain rates. LM features maximize their contribution when the total rain rate is near 3 mm dy^{-1}; however, these features contribute less than 1.1 mm dy^{-1} and, as shown in Fig. 7, while LM's tend to occur in the Subtropics. Over both land and ocean, it is the presence of MCSs, and to a lesser extent SC features, that allow the total rain rate to exceed about 1-2 mm dy^{-1} in most regions, and it is MCSs that allow the total rain rate to exceed 2.5 mm dy^{-1}. These results suggest it may be plausible to parameterize variability in Tropical cloud ensemble populations based upon underlying surface and total rain rate, especially if the variability about the mean trends can be understood. Such parameterizations would be useful as a constraint in rain rate and latent heating distributions.

Acknowledgements

This research was supported by NASA Precipitation Science Funding from under the direction of Dr. Ramesh Kakar. Thanks go to Dr. Daniel Cecil, Dr. Chuntao Liu, Prof. Edward Zipser, Prof. Robert A. Houze, Jr., and Dr.

Timothy Lang for helpful science discussions, and Paul Hein and Margi Cech for administrative support. Special thanks go to Drs. Erich Stocker and John Kwiatkowski and the rest of the TRMM Science Data and Information System (TDSIS) at NASA Goddard Space Flight Center, Greenbelt, MD, for running our software on the TRMM data.

6. References

Biondini, R., 1976: Cloud motion and rainfall statistics. *J. Appl. Meteor.,* **15,** 205–224.

Cecil, D. J., S. J. Goodman, D. J. Boccippio, E. J. Zipser, and S. W. J. Nesbitt, 2005: Three years of TRMM precipitation features. Part I: Radar, radiometric, and lightning characteristics. *Mon. Wea. Rev.*, **133**, 543-566.

Christian, H. J., and Coauthors, 2003: Global frequency and distribution of lightning as observed from space by the Optical Transient Detector. *J. Geophys. Res.*, **108**, 4005, doi:10.1029/2002JD002347.

DeMott, C. A., and Rutledge S. A., 1998a: The vertical structure of TOGA COARE convection. Part I: Radar echo distributions. *J. Atmos. Sci.,* **55**, 2730–2747.

Fritsch, J. M., R. J. Kane, and C. R. Chelius, 1986: The contribution of mesoscale convective weather systems to the warm-season precipitation in the United States. *J. Climate Appl. Meteor.,* **25,** 1333–1345.

Hartmann, D. L., H. H. Hendon, and R. A. Houze Jr., 1984: Some implications of the mesoscale circulations in tropical cloud clusters for large-scale dynamics and climate. *J. Atmos. Sci.,* **41,** 113–121.

Hitchfeld, W. F., and J. Bordan, 1954: Errors inherent in the radar measurement of rainfall at attenuating wavelengths. *J. Meteor.*, **11**, 58–67.

Houze, Jr., R. A., 1989: Observed structure of mesoscale convective systems and implications for large-scale heating. *Quart. J. Roy. Meteor. Soc.,* **115,** 425–461.

——, and C. Cheng, 1977: Radar characteristics of tropical convection observed during GATE: Mean properties and trends over the summer season. *Mon. Wea. Rev.,* **105,** 964–980.

——, and A. K. Betts, 1981: Convection in GATE. *Rev. Geophys. Space Phys.,* **19,** 541–576.

——, 1993: *Cloud Dynamics*. Academic Press, 573 pp.

Iguchi, T., and R. Meneghini, 1994: Intercomparison of single-frequency methods for retrieving a vertical rain profile from airborne or spaceborne radar data. *J. Atmos. Oceanic Technol.,* **11**, 1507–1517.

——, T. Kozu, R. Meneghini, J. Awaka, and K. Okamoto, 2000: Rain-profiling algorithm for the TRMM precipitation radar. *J. Appl. Meteor.,* **39**, 2038–2052.

Johnson, R. H., Rickenbach T. M., Rutledge S. A., Ciesielski P. E., and Schubert W. H., 1999: Trimodal chaacteristics of tropical convection. *J. Climate.,* **12**, 2397–2418.

Keenan, T. D., and Carbone R. E., 1992: A preliminary morphology of precipitation systems in tropical northern Australia. *Quart. J. Roy. Meteor. Soc.*, **118**, 283–326.

Kummerow, C. D., W. Barnes, T. Kozu, J. Shiue, and J. Simpson, 1998: The Tropical Rainfall Measuring Mission (TRMM) sensor package. *J. Atmos. Oceanic Technol.,* **15,** 809–817.

——, and coauthors, 2000: The status of the Tropical Rainfall Measuring Mission (TRMM) after two years in orbit. *J. Appl. Meteor.*, **39**, 1965-1982.

——, and coauthors, 2001: The evolution of the Goddard profiling algorithm (GPROF) for rainfall estimation from passive microwave sensors. *J. Appl. Meteor.,* **40**, 1801–1820.

López, R. E., 1976: Radar characteristics of the cloud populations of tropical disturbances in the northwest Atlantic. *Mon. Wea. Rev.,* **104,** 268–283.

——, 1977: The lognormal distribution and cumulus cloud populations. *Mon. Wea. Rev.,* **105,** 865–872.

——, 1978: Internal structure and development processes of C-scale aggregates of cumulus clouds. *Mon. Wea. Rev.,* **106,** 1488–1494.

Lucas, C., Zipser E. J., and Ferrier B. S., 2000: Sensitivity of tropical West Pacific oceanic squall lines to tropospheric wind and moisture profiles. *J. Atmos. Sci.*, **57**, 2351–2373.

Machado, L. A. T., and Rossow W. B., 1993: Structural characteristics and radiative properties of tropical cloud clusters. *Mon. Wea. Rev.,* **121**, 3234–3260.

Mapes, B. E., and Houze R. A., 1993: Cloud clusters and superclusters over the oceanic warm pool. *Mon. Wea. Rev.,* **121**, 1398–1415.

Miller, J. R., A. S. Dennis, J. H. Hirsch, and D. E. Cain, 1975: Statistics of shower echoes in western North Dakota. Preprints, *16th Radar Meteorology Conf.,* Houston, TX, Amer. Meteor. Soc., 391–396.

Nesbitt, S. W., E. J. Zipser, and D. J. Cecil, 2000: A census of precipitation features in the Tropics using TRMM: Radar, ice scattering, and lightning observations. *J. Climate*, **13**, 4087-4106.

——, and ——, 2003: The diurnal cycle of rainfall and convective intensity according to three years of TRMM measurements. *J. Climate.,* **16**, 1456–1475.

——, ——, and C. D. Kummerow, 2004: An examination of version 5 rainfall estimates from the TRMM microwave imager, precipitation radar, and rain gauges on global, regional and storm scales. *J. Appl. Meteor.*, **43**, 1016-1036.

Petersen, W. A, and S. A. Rutledge, 2001: Regional variability in tropical convection: Observations from TRMM. *J. Climate*, **14**, 3566–3586.

Rickenbach, T. M., and S. A. Rutledge, 1998: Convection in TOGA COARE: Horizontal scale, morphology, and rainfall production. *J. Atmos. Sci.*, **55**, 2715-2729.

Rickenbach, T. M., 1999: Cloud-top evolution of tropical oceanic squall lines from radar reflectivity and infrared satellite data. *Mon. Wea. Rev.,* **127**, 2951–2976.

Schumacher, C., and R. A. Houze, Jr., 2003a: Stratiform rain in the Tropics as seen by the TRMM precipitation radar. *J. Climate*, **16**, 1739-1756.

——, ——, 2003b: The TRMM Precipitation Radar's view of shallow, isolated rain. *J. Appl. Meteor.,* **42**, 1519–1524.

——, ——, and I. Kraucunas, 2003: The Tropical dynamical response to latent heating estimates derived from the TRMM precipitation radar. *J. Atmos. Sci.*, accepted.

Simpson, J, R. F. Adler, and G. R. North, 1988: A proposed Tropical Rainfall Measuring Mission (TRMM) Satellite. *Bull. Amer. Meteor. Soc.*, **69**, 278-295.

Short, D. A., and K. Nakamura, 2000: TRMM radar observations of shallow precipitation over the tropical oceans. *J. Climate*, **23**, 4107-4124.

Spencer, R. W., H. M. Goodman, and R. E. Hood, 1989: Precipitation retrieval over land and ocean with the SSM/I: Identification and characteristics of the scattering signal. *J. Atmos. Oceanic Technol.,* **6,** 254–273.

Takayabu, Y. N., 2002: Spectral representation of rain profiles and diurnal variations observed with TRMM PR over the equatorial area, *Geophys. Res. Lett.*, **29**, doi:10.1029/2001GL014113.

Toracinta, E. R., D. J. Cecil, E. J. Zipser, and S. W. Nesbitt, 2002: Radar, passive microwave, and lightning characteristics of precipitating systems in the Tropics. *Mon. Wea. Rev.,* **130**, 802-824.

Weisman, M. L., and J. B. Klemp, 1984: The structure and classification of numerically simulated convective storms in directionally varying wind shears. *Mon. Wea. Rev.,* **112,** 2479–2498.

Williams, M., and R. A. Houze, Jr., 1987: Satellite-observed characteristics of winter monsoon cloud clusters. *Mon. Wea. Rev.,* **115,** 505–519.

Zipser, E. J., and Lutz K. R., 1994: The vertical profile of radar reflectivity of convective cells: A strong indicator of storm intensity and lightning probability?. *Mon. Wea. Rev.*, **122**, 1751–1759.